Wave Simulations in Ponce de Leon Inlet Using Boussinesq Model

Fengyan Shi[1]; James T. Kirby, M.ASCE[2]; Robert A. Dalrymple, F.ASCE[3]; and Qin Chen[4]

Abstract: An improved curvilinear grid model based on fully nonlinear Boussinesq equations is used to simulate wave propagation in Ponce de Leon Inlet, Fla. We employ the nearshore bathymetry of Ponce de Leon Inlet and generate a stretched curvilinear grid that can resolve shortwaves in the nearshore region and fit the complex geometry. Simulations of 18 cases with monochromatic input waves and Texel-Marsden-Arsloe spectral waves are carried out on the same scale as in the 1:100 scale physical model conducted at the U.S. Army Engineer Research and Development Center. Wave height comparisons, time series comparisons of surface elevation for monochromatic wave cases, and comparisons of power spectrum for spectral wave cases are made between numerical results and laboratory measurements. Comparison is also made between the probability distribution of surface elevation and skewness and asymmetry measures for both the measured data and the Boussinesq model results. It is shown that for the computations of nonlinear wave transformation over irregular bathymetry, the Boussinesq model is able to predict nonlinear wave features and is thus a more accurate model than some conventional models in shallow water.

CE Database subject headings: Boussinesq equations; Numerical models; Finite difference method; Florida; Inlets, waterways.

Introduction

Boussinesq models for surface gravity waves have been shown to provide accurate tools for simulations of wave evolution in coastal regions. Recent advances both in improved dispersion relationships in relatively deep water (Madsen and Sørensen 1992; Nwogu 1993) and in computer technology allow the use of Boussinesq models in large nearshore regions. The incorporation of wave breaking and wave runup into Boussinesq models (Karambas and Koutitas 1992; Schäffer et al. 1993; Madsen et al. 1997; Veeramony and Svendsen 2000; Kennedy et al. 2000; Chen et al. 2000a) also allows these models to be applied to surf zones and swash zones. In addition, Boussinesq models with either structured curvilinear grids or unstructured grids have been developed for application to complex nearshore domains. Sørensen and Sørensen (2000) developed a finite-element Boussinesq model based on the equations derived by Madsen and Sørensen (1992). A finite-element model and a finite-difference curvilinear model based on Beji and Nadaoka's (1996) equations were developed by Li et al. (1999) and Li and Zhan (2001). Shi et al. (2001) developed a finite-difference Boussinesq model in generalized curvilinear coordinates based on the fully nonlinear Boussinesq equations of Wei et al. (1995). Spatially varying and boundary-fitted grids were adopted in the case studies of the model that showed, when compared to the Cartesian version of the Boussinesq model, the curvilinear model has better efficiency and capability to deal with complex geometry in complicated nearshore domains. A literature review on a number of recent developments of Boussinesq models and applications to nearshore wave propagation, surf zone processes and wave-induced currents is given by Kirby (2002).

Recently, a 1:100-scale physical model was constructed at the U.S. Army Engineer Research and Development Center based on the nearshore bathymetry surveyed at Ponce de Leon Inlet, Fla. The inlet is flanked by a 1,295-m north jetty and a south jetty that extends approximately 120 m from the mean low-water contour. The physical model was built to study proposed changes to the north and south jetty configurations and, thus, a series of experimental studies of wave transformation was conducted in the model. Smith and Harkins (1997) evaluated the performances of three numerical wave models—RCPWAVE, REF/DIF-1, and STWAVE—in their studies using the experimental data. It was found that model errors increase markedly with increases in wave nonlinearity, because the three numerical models are basically linear models in shallow water.

In this paper, a Boussinesq model is used to carry out a study of nonlinear wave propagation in Ponce de Leon Inlet. For wave computations in such a large computational domain, with approximate dimensions of $2,500 \times 4,000$ m (prototype) and with a complicated geometry, the generalized curvilinear Boussinesq model shows some advantages. First, a curvilinear grid with stretched grid sizes is able to resolve a broad spectrum of waves in the whole computational domain with good computational efficiency. Secondly, the grid can be a nonorthogonal grid, fitting the complicated geometry well. Starting with the curvilinear Boussinesq model developed by Shi et al. (2001), several improvements are made in the present paper to deal with wave breaking, Smagorinsky subgrid turbulence mixing, and wave

[1]Research Associate, Center for Applied Coastal Research, Univ. of Delaware, Newark, DE 19716. E-mail: fyshi@coastal.udel.edu

[2]Professor, Center for Applied Coastal Research, Univ. of Delaware, Newark, DE 19716.

[3]Professor, Dept. of Civil Engineering, The Johns Hopkins Univ., Baltimore, MD 21218.

[4]Professor, Dept. of Civil Engineering, Univ. of South Alabama, Mobile, AL 36688.

runup/rundown. Corrections for missing small terms are made following Chen et al. (2000b). A Texel-Marsden-Arsloe (TMA) spectral wavemaker is implemented in the model for simulations of irregular waves. The improved model is then used in 18 cases that include monochromatic waves and directional spectral waves. Snapshots of instantaneous water surfaces illustrate wave refraction, diffraction, reflection, and other nonlinear wave features in the complicated domain. The calculated wave heights are compared with measured data at gauge points in two measurement arrays. Spectral analysis for both numerical results and measurement data is carried out. The probability distributions of surface elevations and wave skewness and asymmetry for strong nonlinear-wave cases are computed, and comparisons are made between numerical results and measurement data to demonstrate the capability of the present model for nearshore nonlinear waves.

Model Improvements

The curvilinear Boussinesq model of Shi et al. (2001) is further improved for this study by implementing the corresponding curvilinear terms into the model, following the existing techniques used for wave breaking, runup/rundown, and Smagorinsky-type subgrid mixing (Chen et al. 1999a, 2000a), and the corrections (Chen et al. 2000b) for missing small terms associated with vorticity convection in Wei et al. (1995). The detailed description of those curvilinear representations can be found in the Appendix.

A TMA shallow-water wave spectrum (Bouws et al. 1985) and a wrapped-normal directional-spreading function (Borgman 1984) are used to simulate a directional sea state in the present model. The combined spectrum function can be expressed as

$$S(f,h,\theta) = E_{\text{TMA}}(f,h)G(\theta) \qquad (1)$$

In Eq. (1), E_{TMA} is the TMA shallow-water frequency distribution as follows

$$E_{\text{TMA}}(f,h) = \alpha g^2 f^{-5}(2\pi)^{-4}\Phi(2\pi f,h)e^{-5/4(f/f_p)^{-4}}$$
$$\times \gamma^{e^{[-(f/f_p-1)^2/2\sigma^2]}} \qquad (2)$$

in which f_p is peak frequency, γ presents a frequency spreading parameter which is varied in both the laboratory experiments and the present numerical simulations, and α and σ are coefficients which may be found in Bouws et al. (1985). In this paper, $\alpha = 8 \times 10^{-3}$ and

$$\sigma = \begin{cases} 0.007 & \text{if } f \leqslant f_p \\ 0.09 & \text{if } f > f_p \end{cases}$$
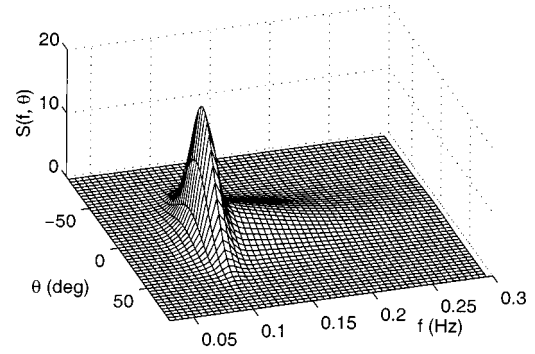
Φ may be expressed as

$$\Phi(2\pi f,h) = \begin{cases} \dfrac{1}{2}\omega_h^2 & \text{for } \omega_h \leqslant 1 \\ 1 - \dfrac{1}{2}(2-\omega_h)^2 & \text{for } 2 > \omega_h > 1 \\ 1 & \text{for } \omega_h \geqslant 2 \end{cases}$$

where

$$\omega_h = 2\pi f\left(\frac{h}{g}\right)^{1/2}$$

$G(\theta)$ is the wrapped-normal directional-spreading function written as

$$G(\theta) = \frac{1}{2\pi} + \frac{1}{\pi}\sum_{n=1}^{N} e^{[-(n\sigma_\theta)^2/2]}\cos n\theta \qquad (3)$$

Fig. 1. TMA directional spectrum ($f_p = 0.1$ Hz, $H_{mo} = 1.0$ m, $\gamma = 5$ and $\sigma_\theta = 20$)

where σ_θ denotes circular deviation of the wrapped-normal spreading function. To avoid the computational underflow, $N \leqslant 10/\sigma_\theta$ in the present paper. Fig. 1 shows a case of TMA directional spectral distribution with $f_p = 0.1$ Hz, $H_{mo} = 1.0$ m, $\gamma = 5$, and $\sigma_\theta = 20$.

The directional spectrum is divided into 2,100 components with random phases and equal energy at each frequency block. The source function technique (Wei et al. 1999) is then used for each component and the final surface elevation function can be written as

$$\eta = \sum_{m=1}^{M} C_m \cos \omega_m t + \sum_{m=1}^{M} S_m \sin \omega_m t \qquad (4)$$
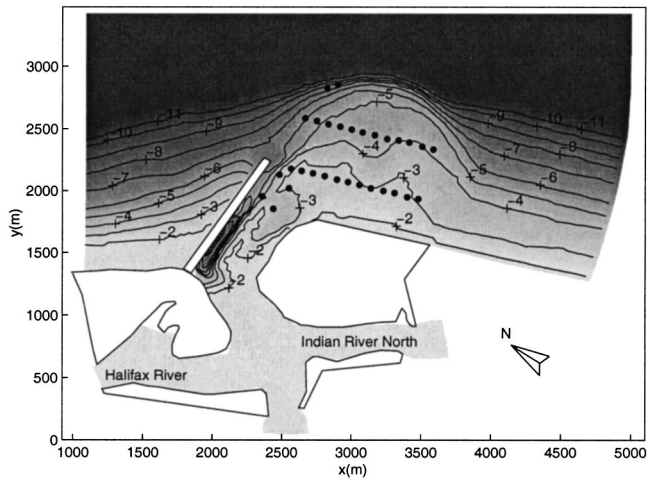
where

$$C_m = \sum_{n=1}^{k} D_{mn}\cos(k_{mn}x + \varepsilon_{mn})$$

$$S_m = \sum_{n=1}^{k} D_{mn}\sin(k_{mn}x + \varepsilon_{mn}) \qquad (5)$$

in which x-axis is oriented along the main axis of the wavemaker; and D_{mn}, k_{mn}, and ε_{mn} are, respectively, the amplitude, wave number, and phase of a component.

Model Setup

The nearshore bathymetry at Ponce de Leon Inlet is complex with the presence of a large ebb shoal, navigation channel, jetties, and inlet leading to the Halifax and Indian Rivers. The bathymetry, shown in Fig. 2, was represented in a 1:100-scale physical model located at the U.S. Army Engineer Research and Development Center. The north jetty was represented by an impermeable vertical structure with small stone sloped on either side. The south jetty was not included in the physical model. Wave data were collected with 30 wave guages, shown in Fig. 2 (dots), at a sampling frequency of 25 Hz. Two gauges were placed immediately shoreward of the depth transition (G-1, G-2) and four were placed in the lee of the jetty (J-1–J-4). Twenty-four gauges were placed in two linear arrays. One array was positioned across the outer lobe of the ebb shoal (offshore array, O-1–O-12 from north to south) and another closer to shore (nearshore array, N-1–N-12
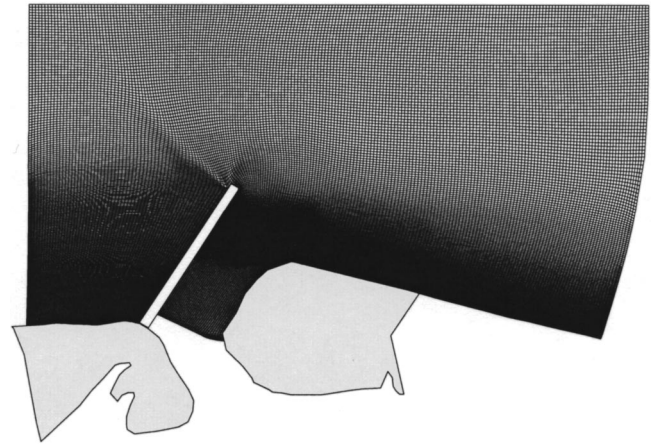
Fig. 2. Bathymetry at Ponce de Leon Inlet (depths in meters, circles represent wave gauges)

Fig. 3. Computational grid (note: real grid resolution is two times higher than that in this demonstration figure)

from north to south). To avoid significant diffraction effects within the gauge array, incident wave directions were limited to ±30° from a line perpendicular to the wave generator. Wave reflections from the model boundaries were minimized by placement of energy-absorbing matting along both lateral boundaries. The bathymetry for numerical models used in Smith and Harkins (1997) is derived from a 1994 airborne lidar survey and partial measurements in the physical model. This bathymetry is also used in the present Boussinesq model.

The numerical calculations are performed on the laboratory scale and the prototype scale is used for model description in this paper to be consistent with Smith and Harkins (1997). A boundary-fitted grid is generated and shown in Fig. 3. The grid-generation method is based on Brackbill and Saltzman's (1982) theory. The corresponding grid-generation software can be downloaded from ⟨http://www.coastal.udel.edu/~fyshi/gridmk/gridhome.html⟩. In this study, we generate a nonorthogonal grid that fits the jetty and shoreline perfectly. The grid resolution is adjusted by using variable grid-density coefficients (Brackbill and Saltzman 1982). A finer resolution is generated near the jetty, the ebb shoal, coastlines and the inlet to resolve structures and short waves in shallow water. The dimension of the generated grid is 401×781. The minimum grid size is 1.39 m near the shoreline on the right side of the jetty and the maximum grid size in the offshore is 5.4 m. The stretched curvilinear grid is able to resolve short waves with a resolution of at least 14 calculation points per wave length in this study.

The numerical wavemaker is located in the same place as in the physical model. The width of the wave-generation region is about one wavelength (peak wavelength for spectral wave cases) as used in Wei et al. (1999). In contrast to the physical model, there is no waveguide at lateral boundaries in the numerical model. To reduce wave diffraction from the wavemaker for obliquely incident wave cases, the length of wavemaker is larger than that in the physical model. A sponge layer is used behind the numerical wavemaker to absorb waves behind the wavemaker. To minimize reflected waves from lateral boundaries and the artificial boundary inside the inlet, sponge layers are put at the same boundaries as in the laboratory experiments. Relatively thin (five point) sponge layers are also used around the jetty and the inlet beach to partially absorb waves. It is found that the thin sponge layers could not absorb waves efficiently on the front side of the

jetty. On the lee side, waves are weak and thus the waves reflected from the jetty do not significantly affect the results at the measurement gauges.

A total of 18 cases with monochromatic input waves and TMA spectral waves are carried out in this study. Table 1 presents a list of incident wave conditions generated in the numerical model. The wave heights listed in the table are significant wave heights H_s for monochromatic waves and H_{mo} for spectral waves. There were 26 cases carried out in the physical model study. Generally, a typical case from the cases with the similar incident wave conditions, was chosen. The cases with very large wave heights were skipped because there was some difficulty in generating ideal incident waves by using the numerical wavemaker. The two-way numerical wavemaker is suspected as causing the problem, because the wave heights generated inside the source region are too large.

For monochromatic wave cases, we specify incident wave height, wave angle, and wave period as the model input. For spectral wave cases, we input wave-peak frequency f_p, H_{mo}, main-incident wave direction, as well as TMA parameters γ and σ_0 described previously. Each case is run for about 150–200 peak wave periods. The time steps used in the model are 0.1 s for all cases, which guarantees that the Courant numbers are less than 0.5 everywhere. On a Linux-based PC with a single CPU of 1.9 GHz and a memory of 1 GB, it takes about 103 h to calculate 200 waves with a wave period of 10 s. Surface elevations at the 30-gauge locations are output every time step during each model run. The time series are used for data analysis after removing the first 500 s of the results.

Model Results and Model/Data Comparisons

Monochromatic Waves

A total of nine monochromatic wave cases were simulated using the curvilinear Boussinesq model. These wave conditions include 8, 10, and 15 s prototype wave periods with wave directions of the negative y-axis and ±30 degrees from the negative y-axis (Cases 1, 3, 6, 7, 9, 11, 13, 15, and 17 from Table 1).

Fig. 4 is a snapshot of surface elevation of normally incident monochromatic waves with a period of 10 s (Case 7). It clearly shows the wave reflection on the up-wave side of the jetty, wave

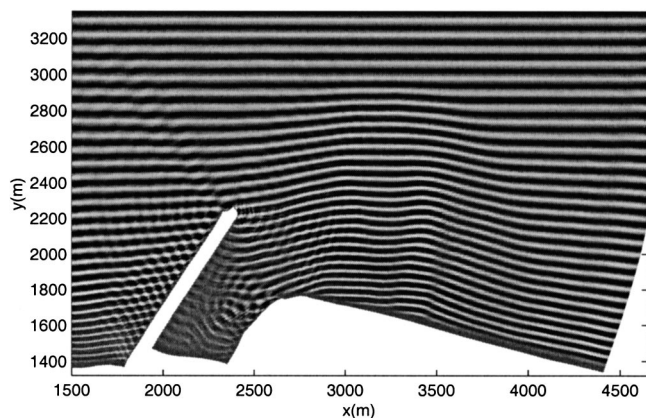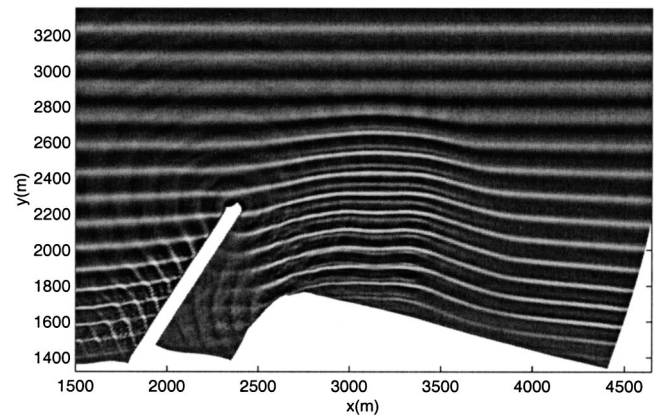**Table 1.** Cases with Different Incident Wave Conditions

Case	H_{mo}/H_s(m)	T(s)	$\theta(°)$[a]	γ[b]	$\sigma_\theta(°)$[c]
01	0.95	8	0	Mono[d]	—
02	1.01	8	0	3.3	30
03	1.15	8	−30	Mono[d]	—
04	1.05	8	−30	3.3	30
05	1.05	8	30	3.3	30
06	1.32	8	30	Mono[d]	—
07	0.93	10	0	Mono[d]	—
08	0.95	10	0	5.0	20
09	0.87	10	−30	Mono[d]	—
10	0.93	10	−30	5.0	20
11	0.74	10	30	Mono[d]	—
12	0.84	10	30	5.0	20
13	0.78	15	0	Mono[d]	—
14	0.98	15	0	7.0	10
15	0.90	15	−30	Mono[d]	—
16	0.73	15	−30	7.0	10
17	0.77	15	30	Mono[d]	—
18	0.76	15	30	7.0	10

[a]Incident wave angle.

[b]Frequency-spreading parameter.

[c]Circular deviation of wrapped-normal-spreading function.

[d]Monochromatic wave.

diffraction on the leeward side, wave scattering from the tip of the jetty, and refractive wave focusing in the area to the right of the inlet mouth. Fig. 5 is a wave pattern of normally incident waves with a long period of 15 s (Case 13). The same reflection, diffraction, and focusing features can be found in the figure. In addition, this long-period wave case illustrates a nonlinear feature represented by the significant secondary wave crests shown to the right of the jetty.

Figs. 6 and 7 compare measured and modeled significant wave heights at the two linear arrays for the two cases with normally incident waves. As demonstrated in Figs. 4 and 5, both measurements and numerical results show the focusing feature indicated by wave height amplifications in the offshore array and nearshore array.
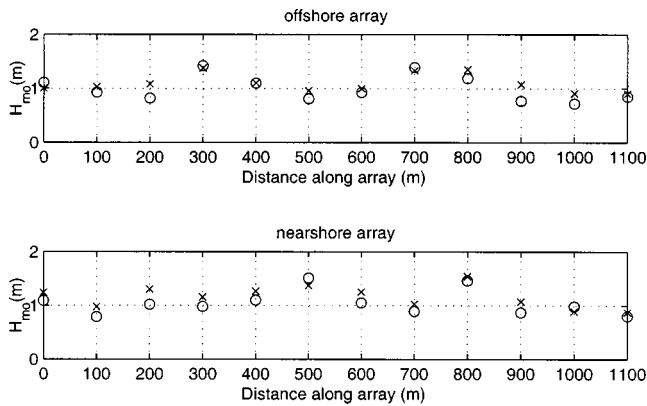
Model/data comparisons of time series of surface elevations are carried out at measurement gauges along the offshore and nearshore arrays. The gauge closest to the wave generator (G-2) is

**Fig. 5.** Snapshot of wave surface elevation (Case 13, $H=0.78$, $T=15$ s, and $\theta=0$)

chosen as a reference for aligning time axes in laboratory and numerical simulations. Figs. 8 and 9 present model/data comparisons of time series of surface elevations in Case 13 at wave gauges along the offshore array (O-1, O-6, O-9, and O-12) and along the nearshore array (N-1, N-6, N-9, and N-12), respectively. Generally, good agreement is found in both figures, although a slight discrepancy in timing of wave-crest arrivals is observed at both the offshore and nearshore arrays. It can be seen from the figures that the secondary wave crests are clearly present at gauges O-6, O-9, N-6, N-9, and N-12 in both the measurements and the numerical results. Similar results are obtained in comparisons of time series of surface elevations for other monochromatic waves cases and are not shown in the paper.

To demonstrate the model performance in representing wave diffraction, we make model/data comparisons at the four gauges in the lee of the jetty. Fig. 10 shows the comparisons of time series of surface elevations in Case 13 ($\theta=0$) at the four gauges—J-1, J-2, J-3, and J-4. The strong diffraction effect of the long-period waves ($T=15$ s) is represented at gauges J-1 and J-2 in both the measurements and the numerical results. At J-3 and J-4, waves with very small wave height are found in the numerical results, while no obvious wave signals are observed in the measurements. The weak wave signals in the numerical results are the reflected waves from the inlet beach on the opposite side of the jetty and can be clearly seen in Fig. 5. The thin sponge layer put on the inlet beach is not very efficient to absorb waves.


Fig. 4. Snapshot of wave surface elevation (Case 7, $H=0.93$, $T=10$ s, and $\theta=0$)
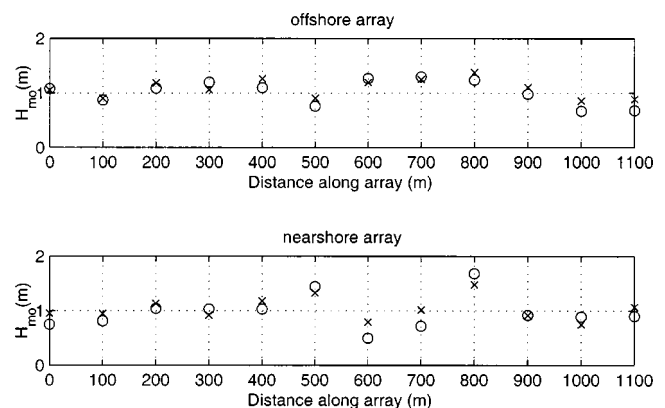
Fig. 6. Wave height comparisons (Case 7, $H=0.93$, $T=10$ s, and $\theta=0$; circles: measurements; crosses: numerical results)
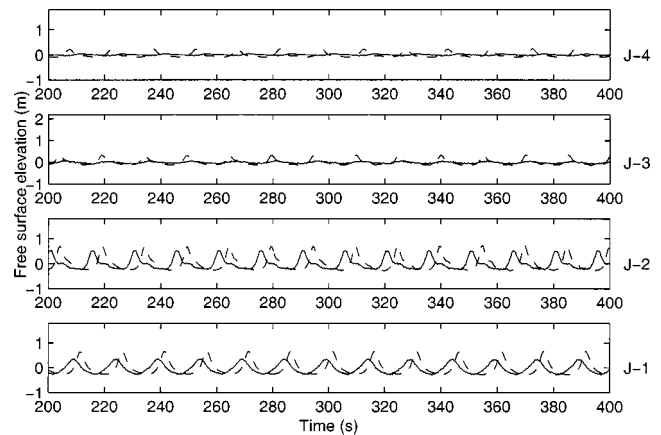
Fig. 7. Wave height comparisons (Case 13, $H = 0.78$, $T = 15$ s, and $\theta = 0$; circles: measurements; crosses: numerical results)
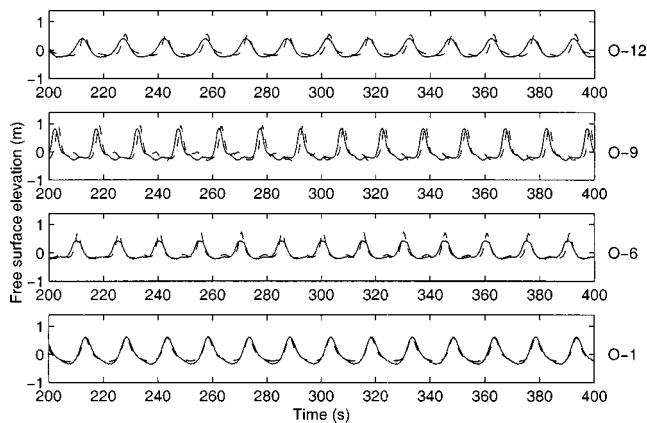
Fig. 8. Comparison of time series of surface elevations at offshore array (Case 13, $H = 0.78$, $T = 15$ s, and $\theta = 0$; dashed line: numerical results; solid line: measurements)
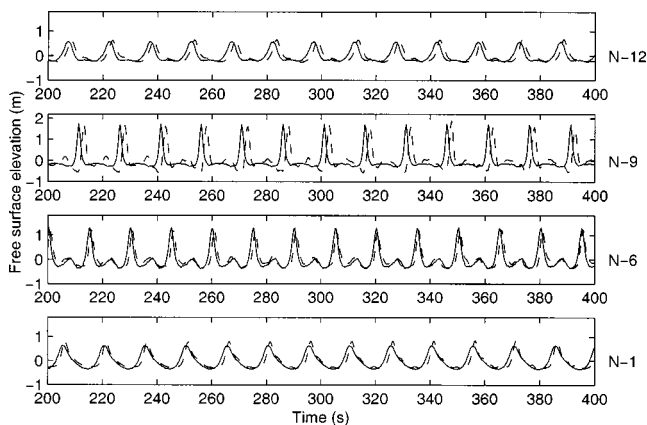
Fig. 9. Comparison of time series of surface elevations at nearshore array (Case 13, $H = 0.78$, $T = 15$ s, and $\theta = 0$; dashed line: numerical results; solid line: measurements)


Fig. 10. Comparison of time series of surface elevations at four gauges on the lee side of the jetty (Case 13, $H = 0.78$, $T = 15$ s, and $\theta = 0$; dashed line: numerical results; solid line: measurements)

For the obliquely incident wave cases, wave diffraction can be found in the shadow regions, such as the inlet throat as shown in Figs. 11, 12, and 13, which present the fairly good model/data comparisons of wave height in the obliquely incident wave cases (Cases 3 and 6). It is shown that in the nearshore array, the locations of maximum wave heights caused by wave focusing over the shoal shift to the right- or left-hand side corresponding to waves from the northwest or southeast. Wave focusing is not obvious in the offshore array.

Spectral Waves

Similar to monochromatic wave cases, nine spectral wave cases are carried out in the numerical study (Cases 2, 4, 5, 8, 10, 12, 14, 16, and 18 from Table 1). Here, we only analyze some typical spectral wave features obtained from the numerical results and then make wave-height comparisons between model and measurement.

A spectral wave case with a peak period of 15 s (Case 14) is shown in Fig. 14. The figure shows that the short-crested waves offshore become long-crested as they propagate towards shore, and wave refraction and focusing are less obviously demonstrated than in the monochromatic wave cases.
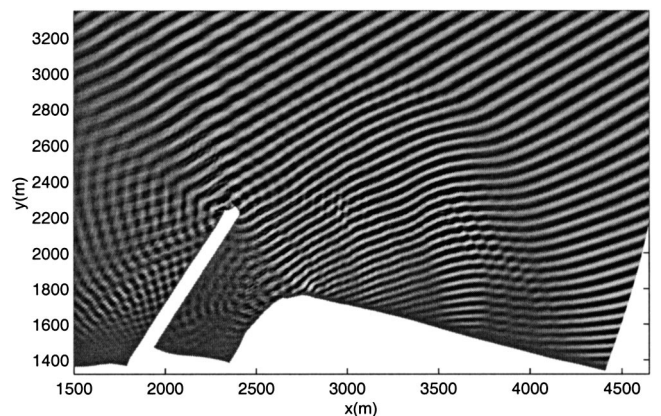
Fig. 11. Snapshot of wave surface elevation (Case 11, $H = 0.74$, $T = 10$ s, and $\theta = 30$)
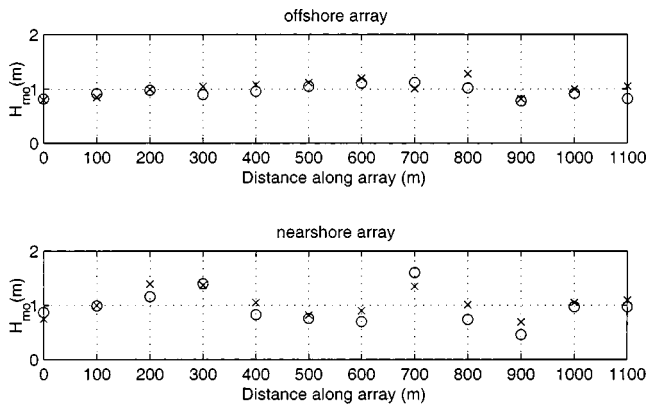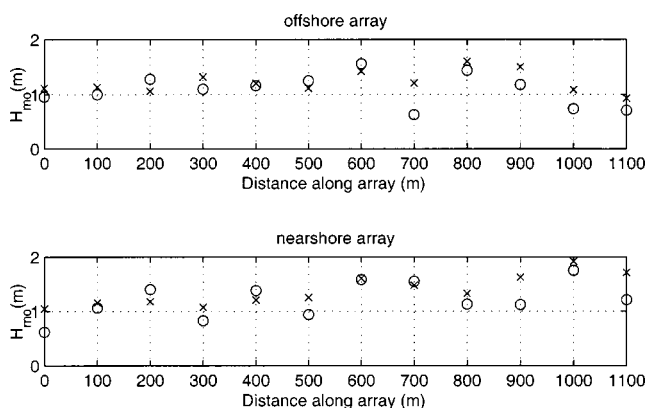
Fig. 12. Wave height comparisons (Case 3, $H = 1.15$, $T = 8$ s, and $\theta = -30$; circles: measurements; crosses: numerical results)

Fig. 14. Snapshot of wave surface elevation (Case 14, $H_{mo} = 0.98$, $T_p = 15$ s, $\theta = 0$, $\gamma = 7.0$, and $\sigma_\theta = 10$)
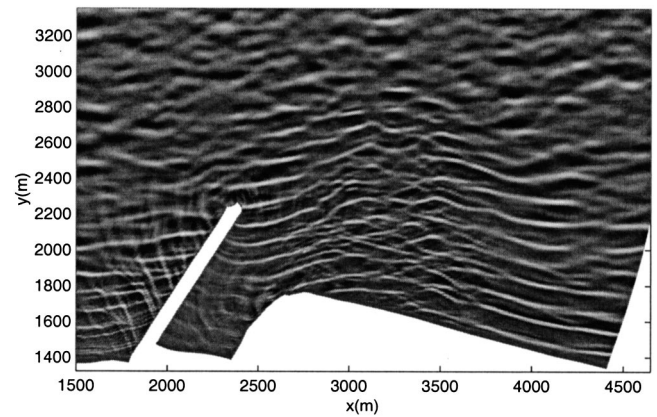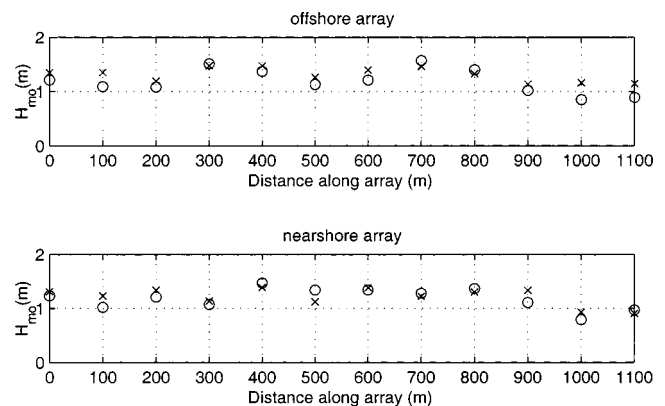
Fig. 14 also demonstrates the good resolution of the stretched curvilinear grid for short waves in the nearshore region. As the improvement of dispersion relationships for Boussinesq equations have expanded their range of validity for wave calculations, the resolution of numerical models becomes of importance especially for spectral wave calculations. In Case 14, the maximum wave frequency in the components employed in the model is 0.13 Hz in prototype, thus, the minimum wavelength in the wave-generation region (water depth = 13 m) is about 75 m that can be resolved by the offshore grid with grid spacing of 5.4 m. Wavelengths become smaller as waves propagate into shallower water. The wave component with the maximum frequency becomes only 33 m long in shallow water of 2 m and even shorter in the shallower water (if we do not consider wave breaking). A finer grid is absolutely needed to resolve the short waves, including short harmonic waves in the shallow-water region. The stretched curvilinear grid with the minimum grid spacing of 1.39 m in the present paper just satisfies the needs.

The wave height H_{mo} comparisons for normally incident wave cases are shown in Figs. 15 and 16. The figures show good agreement between data and model results and also show the smoother wave-height distributions than that in the monochromatic wave cases.

Compared with the monochromatic-wave cases with obliquely incident directions, the oblique spectral waves do not clearly show the effect of diffraction as demonstrated in Fig. 17 because of a wide range of input wave directions. Figs. 18 and 19 compare

modeled wave heights to measured wave heights for peak-incident wave direction of −30° and 30°. General features in wave-height distributions for the spectral wave cases are similar to those of the monochromatic wave cases, such as maximum wave heights shift left or right corresponding to the incident wave angles. As opposed to the monochromatic waves that cause wave focusing to be consistently positioned along the nearshore array, the spectral waves show less wave focusing at the nearshore array due to the superposition of focusing from a wide range of wave periods and directions.

Discussion of Nonlinear Properties

The Boussinesq model is an ideal model for surface gravity wave simulations, because it can predict wave refraction, diffraction, reflection, and most importantly, it can present nonlinear wave features that cannot be predicted by linear models. When waves propagate from deep to shallow water, wave nonlinearity increases with the increase of the Ursell number (1953) $Ur = HL^2/h^3$, where H is wave height; L is wavelength, and h is water depth. The conventional models become invalid when the Ursell number exceeds 40 (Ursell 1953). For the cases with a long period and a large wave height, $T = 15$ s, $H = 0.98$ m, for ex-

Fig. 13. Wave height comparisons (Case 6, $H = 1.32$, $T = 8$ s and $\theta = 30$; circles: measurements; crosses: numerical results)

Fig. 15. Wave height comparisons (Case 14, $H_{mo} = 0.98$, $T_p = 15$ s, $\theta = 0$, $\gamma = 7.0$, and $\sigma_\theta = 10$; circles: measurements; crosses: numerical results)
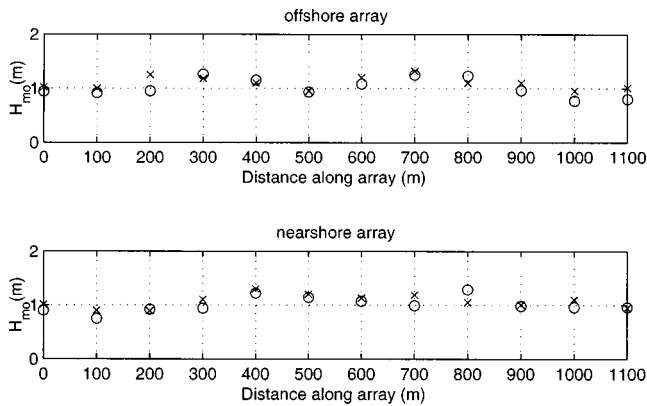
Fig. 16. Wave height comparisons (Case 8, $H_{mo} = 0.95$, $T_p = 10$ s, $\theta = 0$, $\gamma = 5.0$, and $\sigma_\theta = 20$; circles: measurements; crosses: numerical results)

Fig. 18. Wave height comparisons (Case 10, $H_{mo} = 0.93$, $T_p = 10$ s, $\theta = -30$, $\gamma = 5.0$, and $\sigma_\theta = 20$; circles: measurements; crosses: numerical results)

ample, the Ursell number is nearly 40 at offshore array and about 200 at the nearshore array. Conventional wave models are invalid for this case.

The nonlinear wave behavior manifests itself by the generation of higher harmonics in the shoaling region. The Boussinesq prediction of harmonic wave generation and triad interactions have been studied by Madsen and Sørensen (1992), Nwogu (1993), Wei et al. (1995), and Chen et al. (1999b). Wei et al. (1995) demonstrated the importance of high-order nonlinear terms in the fully nonlinear Boussinesq equations for harmonic wave generation. In Fig. 5, we find secondary wave crests due to the release of superharmonics generated by nonlinear shoaling in the nearshore region. Fig. 20 shows the power spectrum at three locations of the offshore array in a spectral wave case (Case 14). All three panels show the apparent second harmonic peaks. Fig. 21 shows the power spectrum at three locations of the nearshore array that indicates the energy transfers towards higher and lower frequencies from the spectral peaks at the offshore array.

Another signature of wave nonlinearity may be indicated by the probability distribution of surface elevation. For a linear wave, the observed sea-surface elevation $\eta(t)$ is normally distributed with mean $\bar{\eta}$ and variance m_0 with the probability-density function PDF(η) taking the form

$$\text{PDF}(\eta) = \frac{1}{\sqrt{2\pi m_0}} e^{-(\eta - \bar{\eta})^2/2m_0} \qquad (6)$$

For a given data set, the probability-density distribution of surface elevation can be computed and its deviation, away from the Gaussian distribution presented in Eq. (6), is a measure of wave nonlinearity of the process. Fig. 22 shows the computed PDF for both the measured data and numerical results at O-1 of the offshore array. There are clear deviations with similar degrees in both the measured data and numerical results, away from the normal distributions. Compared to the normal distribution, there is an excess of extremely large positive values of the function, as well as a deficit of large negative values. This corresponds to the fact that nonlinearity has sharpened the wave crests and flattened the troughs. In addition, there is a deficit of values just above the mean of zero and an excess of values just below. This occurs because of the relatively narrower crests and broader troughs. Fig. 23 shows the computed PDF for waves at N-2 of the nearshore array. It is shown that the stronger nonlinearity in shallow water causes a more significant deviation from the normal distribution.
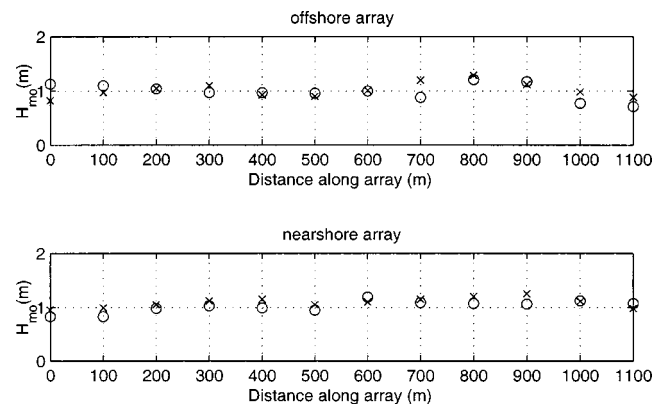
Similarly, wave skewness and asymmetry are also important indicators of nonlinear wave behavior. As waves shoal toward a beach, both skewness and asymmetry increase (asymmetry becomes increasing negative). The prediction of wave skewness is
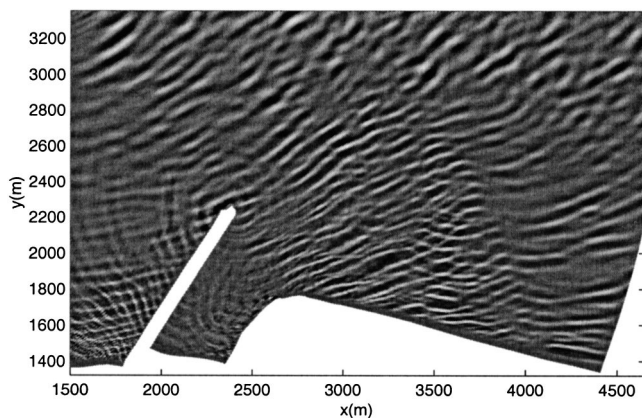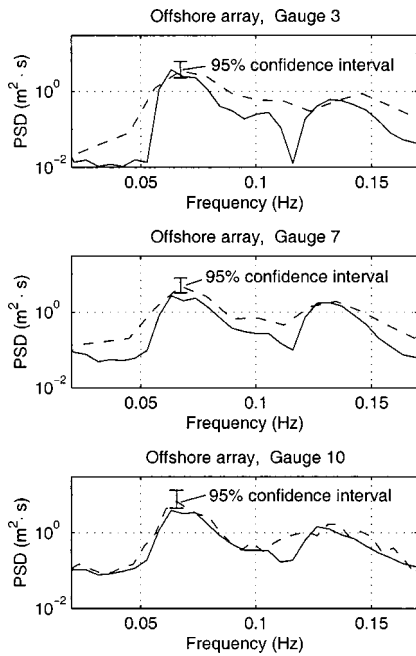

Fig. 17. Snapshot of wave surface elevation (Case 12, $H_{mo} = 0.84$, $T_p = 10$ s, $\theta = 30$, $\gamma = 5.0$, and $\sigma_\theta = 20$)
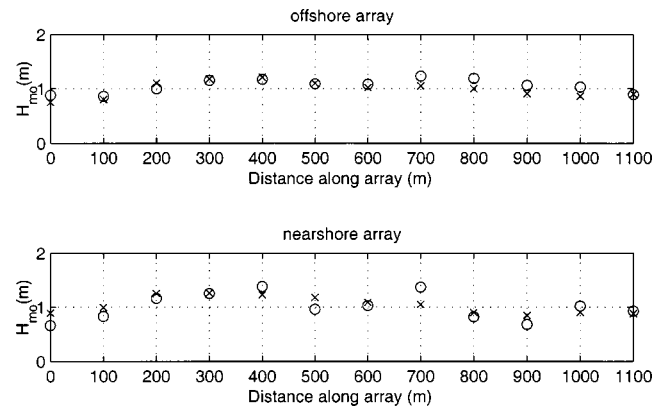

Fig. 19. Wave height comparisons (Case 12, $H_{mo} = 0.84$, $T_p = 10$ s, $\theta = 30$, $\gamma = 5.0$, and $\sigma_\theta = 20$; circles: measurements; crosses: numerical results)

Fig. 20. Power spectrum at O-1, O-5 and O-8 of offshore array (Case 14, $H_{mo}=0.98$, $T_p=15$ s, $\theta=0$, $\gamma=7.0$, and $\sigma_\theta=10$; solid line: measurements; dashed line: numerical results)

important at the viewpoint of sediment transport. Elgar and Guza (1985) have shown that the nonlinear Boussinesq-type model they used for the calculation of shoaling gravity waves is able to predict the sea-surface-elevation skewness of the shoaling wave field. In this paper, wave skewness and asymmetry are computed from time series of surface elevation at the offshore array and nearshore array. Skewness is defined as
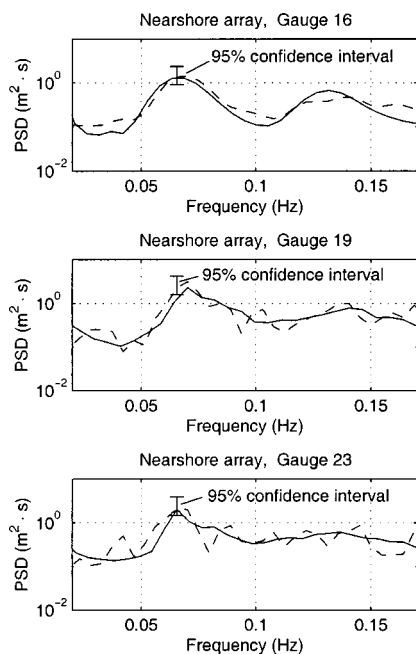
Fig. 21. Power spectrum at N-2, N-5, and N-9 of nearshore array (Case 14, $H_{mo}=0.98$, $T_p=15$ s, $\theta=0$, $\gamma=7.0$, and $\sigma_\theta=10$; solid line: measurements; dashed line: numerical results)
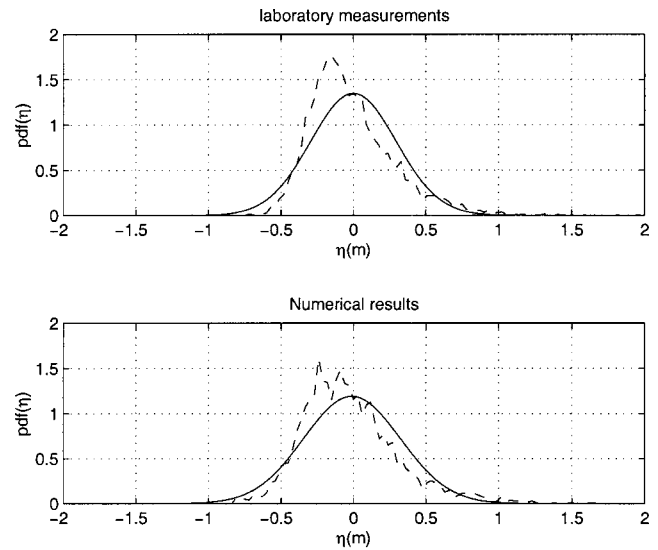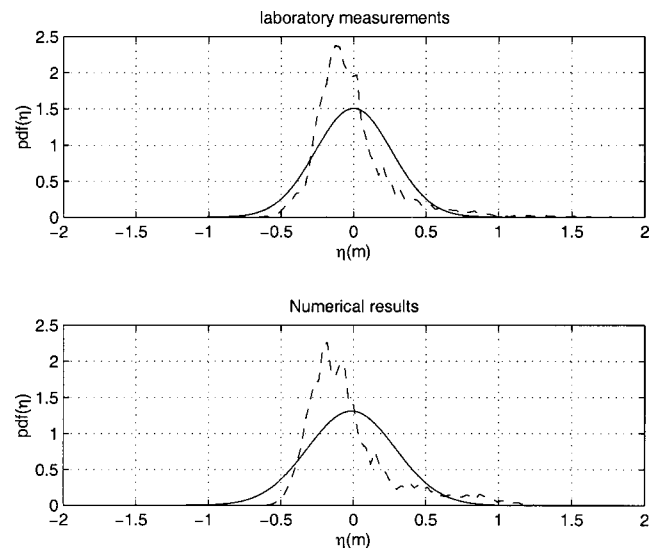

Fig. 22. Probability density distribution of surface elevation at O-1 of offshore array (Case 14, $H_{mo}=0.98$, $T_p=15$ s, $\theta=0$, $\gamma=7.0$, and $\sigma_\theta=10$; solid line: Gaussian distribution; dashed line: PDF distribution of measured data or numerical results)

$$\text{Skewness}=\frac{\langle\eta^3\rangle}{\langle\eta^2\rangle^{3/2}}$$

where $\langle\rangle=$ the averaging operator; and the mean $\bar{\eta}$ has been removed from the time series of surface elevation. Asymmetry is defined as

$$\text{Asymmetry}=\frac{\langle H(\eta)^3\rangle}{\langle\eta^2\rangle^{3/2}}$$

where $H=$ the Hilbert transform and is representative of strong coupling and energy transfer across the frequency spectrum with negative values indicating a transfer of energy from low to high frequencies as in typical shoaling processes.

Fig. 23. Probability density distribution of surface elevation at N-2 of nearshore array (Case 14, $H_{mo}=0.98$, $T_p=15$ s, $\theta=0$, $\gamma=7.0$, and $\sigma_\theta=10$; solid line: Gaussian distribution; dashed line: PDF distribution of measured data or numerical results)
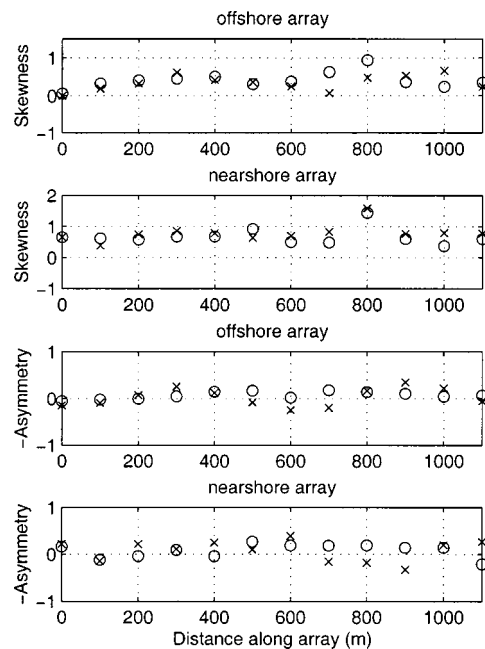
Fig. 24. Comparisons of skewness and asymmetry (Case 01, H = 0.95, T = 8 s, θ = 0; circles: measurements; crosses: numerical results)

Fig. 25. Comparisons of skewness and asymmetry (Case 14, H_{mo} = 0.98, T_p = 15 s, θ = 0, γ = 7.0, and σ_θ = 10; circles: measurements; crosses: numerical results)

A shortwave case (Case 1) is shown in Fig. 24, which compares measured and modeled wave skewness and asymmetry. Skewness is seen to increase as waves propagate from the offshore array to the nearshore array. In both measured and modeled results, large skewness values are found in the corresponding strong shoaling regions around the 800-m points of both the offshore array and the nearshore array. Asymmetry does not increase apparently as waves approach nearshore in the shortwave case. Fig. 25 illustrates comparisons in a long-wave period case (Case 14). In the strong nonlinear wave case, both the numerical results and measured data show that the skewness and asymmetry increase rapidly as waves propagate from the offshore array to the nearshore array. Fig. 25 also shows the overprediction of wave skewness at nearshore array that is caused by unknown reasons.

To quantitatively measure the model/data agreement, RMS error is defined as (Smith and Harkins 1997)

$$\text{RMS}(\%) = \sqrt{\frac{1}{N}\sum_{i=1}^{N}\left(\frac{Hn_i - Hm_i}{Hm_i}\right)^2} \times 100\% \qquad (7)$$

where N = number of data points compared; Hn_i = numerical-model wave height; and Hm_i = measured wave height. To compare to the RMS errors shown in Smith and Harkins (1997), a summary of RMS errors is listed in Table 2 for the cases that were also presented in Smith and Harkins' (1997) paper. We also list the RMS differences in the measurements from the physical model to measure the uncertainties contained in the physical-modeling measurements.

For the monochromatic wave cases, the overall RMS errors from the Boussinesq model are much smaller, especially in the nearshore array, than that from the conventional models. In the nearshore array, RMS errors from RCPWAVE and REF/DIF are over 50% in some cases, because those models are invalid in the strong nonlinear wave region. For the spectral wave cases, the Boussinesq results appear to be only marginally better than the STWAVE results. The reason could be that for broad-band wave
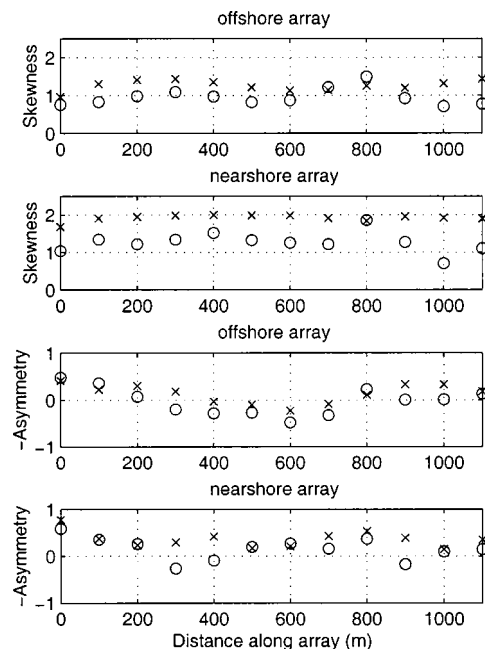
cases, the STWAVE model is able to predict well wave heights. However, we expect that the STWAVE model may not give right spectral distributions in shallow water, because it cannot predict some wave nonlinearities, such as wave harmonics. Although some of the results from the present model are clearly in better agreement with the data, we could not comment on the model accuracy, because a part of the numerical model bathymetry was developed from linearly interpolated depths between design templates, not a postconstruction survey of the concrete beach (Smith and Harkins 1997).

Conclusions

The improved curvilinear Boussinesq model based on the fully nonlinear equations was used to simulate nonlinear waves in Ponce de Leon Inlet, Fla. The curvilinear model can resolve the complex geometry and predict nonlinear wave transformation in the large computational domain. Eighteen cases were calculated and fairly good agreement in the wave-height comparisons were obtained.

Nonlinear wave features were presented in the case study by the fully nonlinear Boussinesq model. Secondary wave-crest patterns were clearly shown in the monochromatic wave cases. Spectral analysis of spectral wave cases also showed the wave-energy transfer from the original peak frequencies to the corresponding harmonic frequencies. As another indicator of wave nonlinearity, the probability distributions of wave surface elevations were computed from both the measured data and numerical results and showed similar deviations from their Gaussian distributions. The good agreements because model and data comparisons of wave skewness and asymmetry indicate the capability of the model to predict nonlinear wave transformation.

Strong wave reflection from the jetty was found in the numerical results, which may not occur in the physical experiments. Further work with a structure boundary condition is needed. We

Table 2. RMS Errors of Wave Heights

Case	RCPWAVE Offshore	RCPWAVE Nearshore	REF/DIF Offshore	REF/DIF Nearshore	STWAVE Offshore	STWAVE Nearshore	BOUSSINESQ Offshore	BOUSSINESQ Nearshore	Gauge Offshore	Gauge Nearshore
01	17	25	15	16	—	—	11.8	17.4	5.3	5.4
02	—	—	—	—	9.6	16	8.0	14.5	0.7	1.4
07	27	66	26	45	—	—	15.4	24.6	3.2	3.1
08	—	—	—	—	9.5	15	10.6	15.7	1.6	2.2
09	13	57	14	58	—	—	13.4	20.9	6.9	6.4
10	—	—	—	—	9.8	17	5.9	13.2	2.2	3.2
11	24	50	17	53	—	—	15.2	21.4	9.1	9.4
12	—	—	—	—	13	5.6	8.3	10.1	1.4	2.1
13	27	38	25	23	—	—	13.6	20.8	4.3	4.9
14	—	—	—	—	12	23	11.4	17.5	3.8	4.0

also encountered difficulty when generating large incident waves with the numerical wavemaker. The wave-generation technique needs to be further improved by using the one-way numerical wavemaker recently developed by Chawla and Kirby (2000), which eliminates the backward propagating wave in the source region and thus reduces problems associated with breaking of two-way waves in that region.

Acknowledgments

Appendix. Curvilinear Implementation of Wave Breaking, Subgrid Mixing, Slot Technique, and Terms Associated with Vorticity Transport

The fully nonlinear Boussinesq equations with corrections for missing small terms can be found in Chen et al. (2000b). After a generalized coordinate transformation (Shi et al. 2001), the equations can be written in the tensor-invariant forms

$$\beta \eta_t + \frac{1}{\sqrt{g_0}} \frac{\partial}{\partial x^k}(\sqrt{g_0} M^k) = 0 \tag{8}$$

$$
\begin{aligned}
M^k = \Lambda \Bigg\{ &(h+\eta)u^k + (h+\eta)\left[\frac{z_\alpha^2}{2} - \frac{1}{6}(h^2 - h\eta + \eta^2)\right] \\
&\times \left[\frac{1}{\sqrt{g_0}}\frac{\partial}{\partial x^l}(\sqrt{g_0}u^l)\right]!^k + (h+\eta)\left[z_\alpha + \frac{1}{2}(h-\eta)\right] \\
&\times \left[\frac{1}{\sqrt{g_0}}\frac{\partial}{\partial x^l}(\sqrt{g_0}hu^l)\right]!^k \Bigg\}
\end{aligned}
\tag{9}
$$

$$\frac{\partial u^k}{\partial t} + g\eta !^k + u^l u^k_{,l} + V_1^k + V_2^k + V_3^k + R_b^k + R_s^k = 0 \tag{10}$$

where k, $l = 1$ and 2; $(u^1, u^2) =$ contravariant components of a reference velocity at a reference elevation z_α; $(x^1, x^2) =$ new independent variables in the transformed image domain; β and Λ = two dimensionless multipliers introduced for the treatment of shoreline run-up; $\sqrt{g_0}$ is the Jacobi value; $()_k$ represents the covariant spatial derivative while $!^k$ represents the contravariant spatial derivative; V_1^k and V_2^k are the dispersive Boussinesq terms that can be found in Shi et al. (2001); and V_3^k represents extra terms associated with vorticity transport (Chen et al. 2000b).

In Eq. (10), R_b^k and R_s^k represent the breaking terms and the subgrid mixing terms, respectively.

Energy Dissipation Due to Wave Breaking and Subgrid Mixing

The energy dissipation due to wave breaking in shallow water is modeled by using the momentum mixing terms, which can be written in a general form as

$$\frac{1}{H}\mathrm{div}(H\nu\mathbf{D}) \tag{11}$$

where $\nu =$ eddy viscosity localized on the front face of the breaking wave (Kennedy et al. 2000; Chen et al. 2000a); $\mathbf{D}$ = rate-of-strain tensor defined by

$$\mathbf{D} = \frac{1}{2}[\mathrm{grad}\,\mathbf{u} + (\mathrm{grad}\,\mathbf{u})^T] \tag{12}$$

in which $(\mathrm{grad}\,\mathbf{u})^T$ is the transpose of $\mathrm{grad}\,\mathbf{u}$. The tensor-invariant forms of the diffusion terms in generalized curvilinear coordinates can be expressed as

$$R_b^k = \frac{1}{H\sqrt{g_0}}\frac{\partial \sqrt{g_0}\nu H D^{ki}}{\partial x^i} + \nu D^{ji}\Gamma_{ji}^k \tag{13}$$

where $\Gamma_{ji}^k =$ Christoffel symbol of the second kind and

$$D^{ij} = \frac{1}{2}(g^{kj}u^i_{,k} + g^{ki}u^j_{,k}) \tag{14}$$

The subgrid mixing terms are in the same form as shown in Eq. (11) except that ν should be replace by the eddy viscosity due to the subgrid turbulence ν_s

$$\nu_s = c\sqrt{g_0}|\mathbf{T}| = c\sqrt{g_0}(T^{ij}T_{ij})^{1/2} \tag{15}$$

where $c =$ subgrid mixing coefficient; $T =$ rate-of-strain tensor of the velocity of the wave-generated current $\mathbf{U}$ which may be obtained by averaging the instantaneous velocity over several wave periods. $\mathbf{T}$ can be written as

$$\mathbf{T} = \frac{1}{2}[\mathrm{grad}\,\mathbf{U} + (\mathrm{grad}\,\mathbf{U})^T] \tag{16}$$

The tensor-invariant forms of the subgrid mixing terms can be written as

$$R_s^k = \frac{1}{H\sqrt{g_0}} \frac{\partial \sqrt{g_0}\nu_s HD^{ki}}{\partial x^i} + \nu_s D^{ji}\Gamma_{ji}^k \qquad (17)$$

where

$$T^{ji} = \frac{1}{2}(g^{kj}U_{,k}^i + g^{ki}U_{,k}^j) \qquad (18)$$

and

$$T_{ij} = \frac{1}{2}(g_{ki}U_{,j}^k + g_{kj}U_{,i}^k) \qquad (19)$$

Slot Technique

Following the rectangular version of the fully nonlinear Boussinesq model (Chen et al. 2000a), a slot technique is implemented in the curvilinear model. The dimensionless multipliers β and Λ in Eqs. (8) and (9) are defined exactly as in Chen et al. (2000a). The implementation is also the same as in the rectangular version except that the slots are always along the curvilinear coordinate lines.

Implementation of Extra Terms Associated with Vorticity Transport

Compared with the Boussinesq equations in Li (1999), Chen et al. (2000b) or Hsiao et al. (2002), the missing terms in Wei et al. (1995) are the $O(\mu^2)$ vorticity terms in the momentum equations and can be expressed as

$$\mathbf{V}_3 = (\mathbf{u} \cdot \nabla z_\alpha)[z_\alpha \nabla(\nabla \cdot \mathbf{u}) + \nabla(\nabla \cdot h\mathbf{u})] - \nabla z_\alpha[(\mathbf{u} \cdot \nabla)(\nabla \cdot h\mathbf{u})$$
$$+ z_\alpha(\mathbf{u} \cdot \nabla)(\nabla \cdot \mathbf{u})] \qquad (20)$$

In a tensor-invariant form, Eq. (20) can be written as

$$V_3^k = u^l \frac{\partial z_\alpha}{\partial x^l}\left[z_\alpha \left(\frac{1}{\sqrt{g_0}} \frac{\partial \sqrt{g_0}u^l}{\partial x^l} \right)^{!k} + \left(\frac{1}{\sqrt{g_0}} \frac{\partial \sqrt{g_0}hu^l}{\partial x^l} \right)^{!k} \right]$$
$$- z_\alpha^{!k}\left[u^l \frac{\partial}{\partial x^l}\left(\frac{1}{\sqrt{g_0}} \frac{\partial \sqrt{g_0}hu^m}{\partial x^m} \right) + z_\alpha u^l \frac{\partial}{\partial x^l}\left(\frac{1}{\sqrt{g_0}} \frac{\partial \sqrt{g_0}u^m}{\partial x^m} \right) \right]$$
$$(21)$$

Based on the definitions in the specific model implementation in Shi et al. (2001), we define F_7 and G_7 for the new extra terms which are expressed as

$$F_7 = -(Uz_{\alpha,\xi_1} + Vz_{\alpha,\xi_2})\frac{1}{g_0}[g_{22}z_\alpha(\mathrm{DU})_{\xi_1} - g_{12}z_\alpha(\mathrm{DU})_{\xi_2}$$

$$+ g_{22}(\mathrm{DHU})_{\xi_1} - g_{12}(\mathrm{DHU})_{\xi_2}] + \frac{1}{g_0}(z_{\alpha,\xi_1}g_{22} - z_{\alpha,\xi_2}g_{12})$$

$$\times [U(\mathrm{DHU})_{\xi_1} + V(\mathrm{DHU})_{\xi_2} + z_\alpha U(\mathrm{DU})_{\xi_1} + z_\alpha V(\mathrm{DU})_{\xi_2}]$$

$$(22)$$

and

$$G_7 = -(Uz_{\alpha,\xi_1} + Vz_{\alpha,\xi_2})\frac{1}{g_0}[-g_{12}z_\alpha(\mathrm{DU})_{\xi_1} + g_{11}z_\alpha(\mathrm{DU})_{\xi_2}$$

$$- g_{12}(\mathrm{DHU})_{\xi_1} + g_{11}(\mathrm{DHU})_{\xi_2}] + \frac{1}{g_0}(-z_{\alpha,\xi_1}g_{12} + z_{\alpha,\xi_2}g_{11})$$

$$\times [U(\mathrm{DHU})_{\xi_1} + V(\mathrm{DHU})_{\xi_2} + z_\alpha U(\mathrm{DU})_{\xi_1} + z_\alpha V(\mathrm{DU})_{\xi_2}]$$

$$(23)$$

The definitions of DU and DHU are the same as in Shi et al. (2001).

References

Beji, S., and Nadaoka, K. (1996). "A formal derivation and numerical modelling of the improved Boussinesq equations for varying depth." *Ocean Eng.,* 23(8), 691–704.

Borgman, L. E. (1984). "Directional spectrum estimation for the S_{xy} gages." *Tech. Rep., CHL-97-24*, United States Army Corps of Engineers (USACE), Waterway Experiment Station.

Bouws, E., Gunther, H., Rosenthal, W., and Vincent, C. L. (1985). "Similarity of the wind spectrum in finite depth water, 1. Spectral form." *J. Geophys. Res.,* 90(NC1), 975–986.

Brackbill, J. U., and Saltzman, J. S. (1982). "Adaptive zoning for singular problems in two dimensions." *J. Comput. Phys.,* 46(3), 342–368.

Chawla, A., and Kirby, J. T. (2000). "A source function method for generation of waves on currents in Boussinesq models." *Appl. Ocean Res.,* 22(2), 75–83.

Chen, Q., Dalrymple, R. A., Kirby, J. T., Kennedy, A., and Haller, M. C. (1999a). "Boussinesq modeling of a rip current system." *J. Geophys. Res.,* 104(20), 617–20, 637.

Chen, Q., Madsen, P. A., and Basco, D. R. (1999b). "Current effects on nonlinear interactions of shallow-water waves." *J. Waterw., Port, Coastal, Ocean Eng.,* 125(4), 176–186.

Chen, Q., Kirby, J. T., Dalrymple, R. A., Kennedy, A. B., and Chawla, A. (2000a). "Boussinesq modeling of wave transformation, breaking, and runup. II: 2D." *J. Waterw., Port, Coastal, Ocean Eng.,* 126(1), 48–56.

Chen, Q., Kirby, J. T., Dalrymple, R. A., Kennedy, A. B., Thornton, E. B., and Shi, F. (2000b). "Boussinesq modeling of waves and longshore currents under field conditions." *Proc., 27th Int. Conf. Coastal Engineering*, Sydney, ASCE, Reston, Va., 651–663.

Elgar, S., and Guza, R. T. (1985). "Shoaling gravity waves: Comparisons between field observations, linear theory, and a nonlinear model." *J. Fluid Mech.,* 158, 47–70.

Hsiao, S., Liu, P. L.-F., and Chen, Y. (2002). "Nonlinear water waves propagating over a permeable bed." *Proc. R. Soc. London, Ser. A,* 458(2022), 1291–1322.

Karambas, T. V., and Koutitas, C. A. (1992). "A breaking wave propagation model based on the Boussinesq equations." *Coastal Eng.,* 18(1-2), 1–19.

Kennedy, A. B., Chen, Q., Kirby, J. T., and Dalrymple, R. A. (2000). "Boussinesq modeling of wave transformation, breaking, and runup. I: 1D." *J. Waterw., Port, Coastal, Ocean Eng.,* 126(1), 39–47.

Kirby, J. T. (2002). "Boussinesq models and applications to nearshore wave propagation, surfzone processes and wave-induced currents." *Advances in coastal engineering.,* V. C. Lakhan, ed., Elsevier Science, New York.

Li, Y. S., and Zhan, J. M. (2001). "Boussinesq-type model with boundary-fitted coordinate system." *J. Waterw., Port, Coastal, Ocean Eng.,* 127(3), 152–160.

Li, Y. S., Liu, S. X., Yu, Y. X., and Lai, G. Z. (1999). "Numerical modeling of Boussinesq equations by finite element method." *Coastal Eng.,* 37(2), 97–122.

Madsen, P. A., and Sørensen, O. R. (1992). "A new form of the Boussinesq equations with improved linear dispersion characteristics, 2. A slowly varying bathymetry." *Coastal Eng.,* 18(3-4), 183–204.

Madsen, P. A., Sørensen, O. R., and Schäffer, H. A. (1997). "Surf zone dynamics simulated by a Boussinesq mode, I. Model description and cross-shore motion of regular waves." *Coastal Eng.,* 32, 255–287.

Nwogu, O. (1993). "Alternative form of Boussinesq equations for near-shore wave propagation." *J. Waterw., Port, Coastal, Ocean Eng.,* 119(6), 618–638.

Schäffer, H. A., Madsen, P. A., and Deigaard, R. A. (1993). "A Bouss-inesq model for waves breaking in shallow water." *Coastal Eng.,* 20(3-4), 185–202.

Shi, F., Dalrymple, R. A., Kirby, J. T., Chen, Q., and Kennedy, A. (2001). "A fully nonlinear Boussinesq model in generalized curvilinear coordinates." *Coastal Eng.,* 42(4), 337–358.

Smith, S. J., and Harkins, G. S. (1997). "Numerical wave model evaluations using laboratory data." *Proc., Ocean Wave Measurement and Analysis, Waves '97*, Virginia Beach, Va., ASCE, Reston, Va., 271–285.

Sørensen O. R., and Sørensen L. S. (2000). "Boussinesq type modelling using unstructured finite element technique." *Proc., 27th Int. Conf. Coastal Engineering*, Sydney, ASCE, Reston, Va., 190–202.

Ursell, F. (1953). "The long-wave paradox in the theory of gravity waves." *Proc., Cambridge Philos. Soc.,* 49(4), 685–694.

Veeramony, J., and Svendsen, I. A. (2000). "The flow in surf zone waves." *Coastal Eng.,* 39(2-4), 93–122.

Wei, G., Kirby, J. T., Grilli, S. T., and Subramanya, R. (1995). "A fully nonlinear Boussinesq model for surface waves, Part 1: Highly nonlin-ear unsteady waves." *J. Fluid Mech.,* 294, 71–92.

Wei, G., Kirby, J. T., and Sinha, A. (1999). "Generation of waves in Boussinesq models using a source function method." *Coastal Eng.,* 36(4), 271–299.